Jefferson Lab

Newport News, VA

GlueX/Hall D Calorimeter Final Design and Safety Review
February 19-20, 2008

Section 2:
BCAL – The Barrel Calorimeter

GlueX/Hall D Calorimeter Conceptual Design Report
Section 2 of 5

2 BCAL: The Barrel Calorimeter

2.1 Overview

As discussed in the introductory section above, the solenoidal geometry of the GLUEX exotic hybrid search experiment drives the need for a cylindrical (barrel-shaped) electromagnetic calorimeter (BCAL) to detect photons and measure their energies and positions. The GLUEX geometry calls for this calorimeter to be approximately 4 m long with a thickness that will fit inside the bore of the solenoid while accommodating a tracking detector around the target. A schematic of BCAL, its placement with respect to the beamline and liquid hydrogen target, BCAL's end view and an end of one of the 48 BCAL modules showing the readout segmentation are all shown in Figure 2.1. More details will be given in what follows.
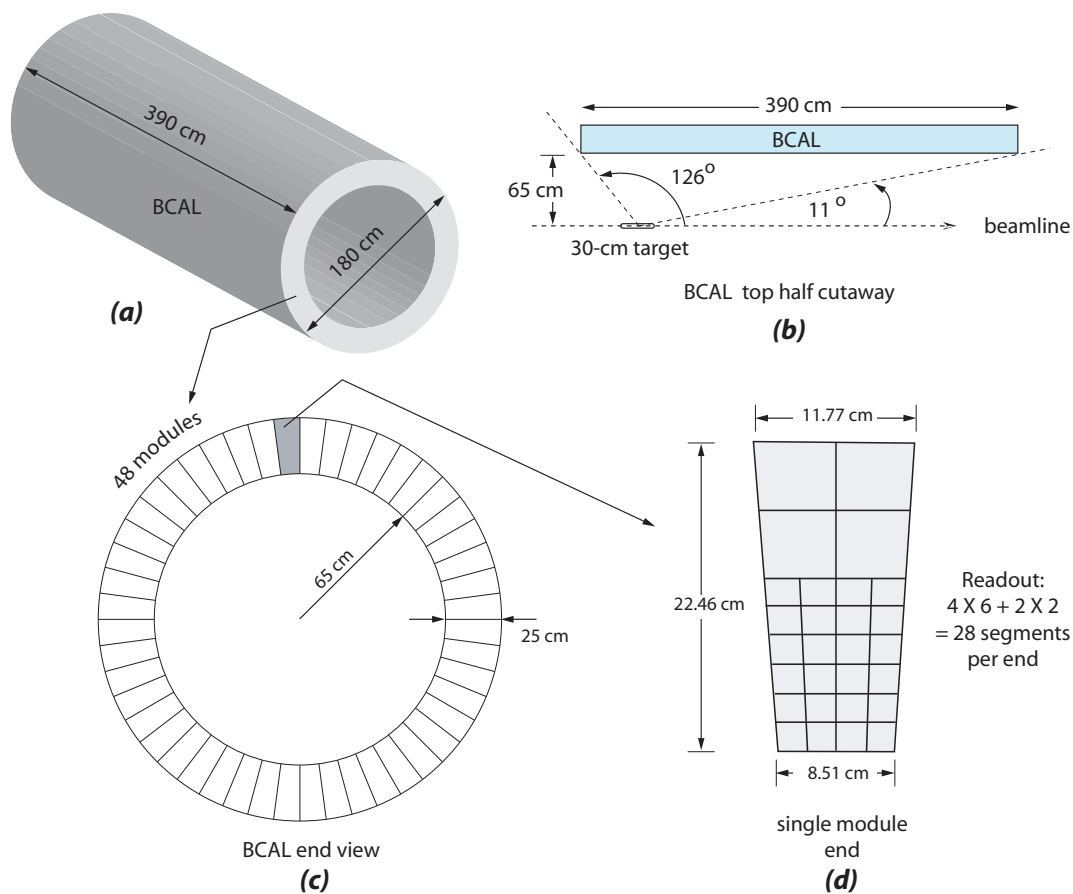

Figure 2.1: The GLUEX BCAL calorimeter. (a) BCAL schematic; (b) top-half cutaway showing the placement of BCAL with respect to the beamline and liquid hydrogen target; (c) BCAL end view showing 48 modules; and (d) end view of a module showing readout segmentation. Details are given in the text.

The electromagnetic detector used in the KLOE detector [1] at DAΦNE [2], the Frascati ϕ-factory, operated in a solenoidal magnetic field. The design of the BCAL has been based, in part, on that of the KLOE electromagnetic calorimeter. The KLOE calorimeter design and performance characteristics are presented in Appendix A. While the BCAL length is only slightly shorter than that of the KLOE calorimeter, its inner

diameter is significantly smaller, 1.3 m compared to 4 m for the latter. However, the important parameters that define energy and timing capabilities are similar. It is important to point out differences in the GLUEX and KLOE applications of the barrel calorimetry. In KLOE, the intersection region is at the center of the calorimeter which, as a result, is illuminated symmetrically, and nearly uniformly, by photons. In GLUEX the 30-cm target is placed near the upstream end of the calorimeter and the vast majority of photons illuminate the section near the downstream end. For KLOE the photon energies are, on average, between 100 and 200 MeV with very few photons greater than 400 MeV in energy while for GLUEX the photon energies are higher. *e.g.* 30% of photons in BCAL will have energies considerably higher than 500 MeV. Despite these differences, the KLOE experience provides valuable guidance in the design and construction of the BCAL calorimeter.

The relevant kinematics for BCAL is captured in Figure 2.2 which shows the expected (a) energy and (b) angular spectra of photons in BCAL based on PYTHIA simulations. In each case the distribution is shown along with the percent integral distribution (use the right axis). Figure 2.2(a), we see that 50%, 30% and 10% of all photons in BCAL have energies greater than 0.25, 0.50 and 1.0 GeV respectively. From Figure 2.2(a), we see that 50% of the photons in BCAL have angles less than 90° and 96% have angles less than 90°. In Figure 2.2(b), the total number of radiation lengths intercepted by a photon, emerging from target center, is also shown. Note the variation of the number of BCAL radiation lengths traversed as a function of photon angle assuming a BCAL thickness of 22.46 cm and a radiation length of 1.45 cm for the Pb/SciFi matrix. At 90° the photons traverse 15.5 radiation lengths. The linear increase from 0 to 62 radiation lengths near 14° corresponds to photon trajectories exiting out the downstream end of BCAL while the linear drop starting at 118° corresponds to trajectories exiting out the upstream end. Figure 2.2(c) shows the correlation of energy with angle of photons. The mean energy as a function of angle is shown as filled markers and the dotted lines represent $\pm\sigma$.
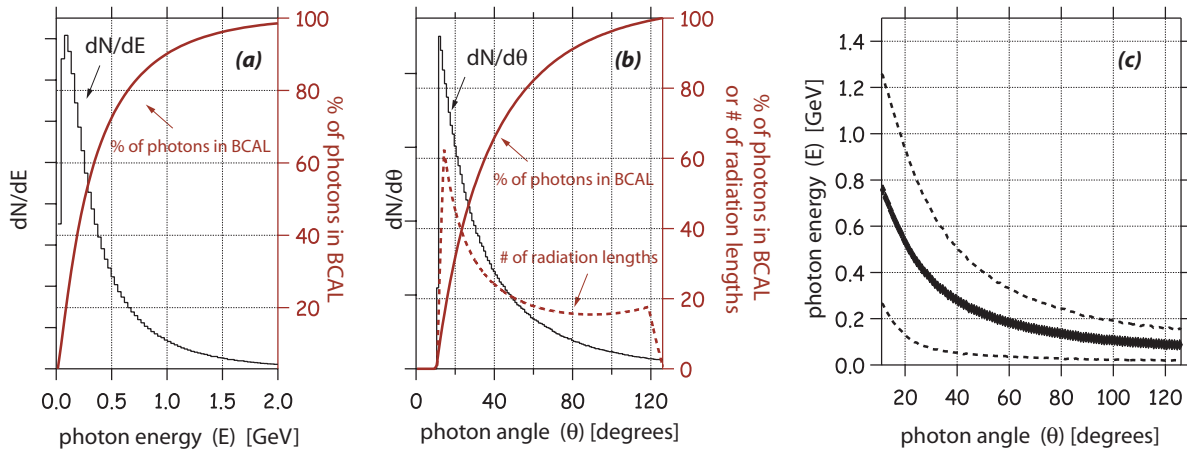

Figure 2.2: Expected (a) energy spectrum, (b) angular spectrum and (c) correlation of energy with angle of photons in BCAL based on PYTHIA simulations. In (a) and (b) the distribution is shown along with the percent integral distribution (use the right axis). In plot (b) the total number of radiation lengths intercepted by a photon, emerging from target center, is also shown. In (c) the mean energy as a function of angle is shown as filled markers and the dotted curves represent the mean $\pm\sigma$.

2.2 BCAL parameters

In the introductory section of this chapter, we showed that the planned overall length, inner radius and segmentation of BCAL (please refer to Figure 2.1) are well matched to the kinematics of fixed target photoproduction at around 8 to 10 GeV. How well BCAL performs, with regard to energy resolution, time difference resolution, mean time resolution, energy threshold and photon reconstruction efficiency, will depend on the details of the design and construction. Table 2.1 summarizes the salient features of BCAL. These design parameters are based on the KLOE experience, on detailed GEANT-based simulations and tests of a full scale prototype in charged particle and photon beams and cosmic rays.

The detailed design of the BCAL modules has already been realized in two full-scale prototype modules (4-m long) and smaller prototypes. Details of the construction of these prototype modules and the techniques to be used for BCAL construction are included in Appendix B. The lead-scintillating matrix that closely follows the KLOE design and is shown schematically in Figure 2.3. It consists of alternating layers of thin (0.5 mm) lead sheets and 1-mm-diameter, dual-clad, scintillating fibers (SciFi) from PolHiTech with peak emission wavelength of 420 nm. The lead sheets were plastically deformed after passing through a specially-designed swaging machine. The fibers are glued manually in the resulting grooves with an optical epoxy. The thickness of the module in radiation lengths is 15.5. The sampling fraction derived from its ~184 layers of SciFi is 12%. The Pb:SciFi:Glue ratios for the module are 37:49:14 leading to a radiation length of 1.45 cm. Details leading to the radiation length estimates are given in [3]. For more details, the reader is directed to references [3, 4, 5, 6].
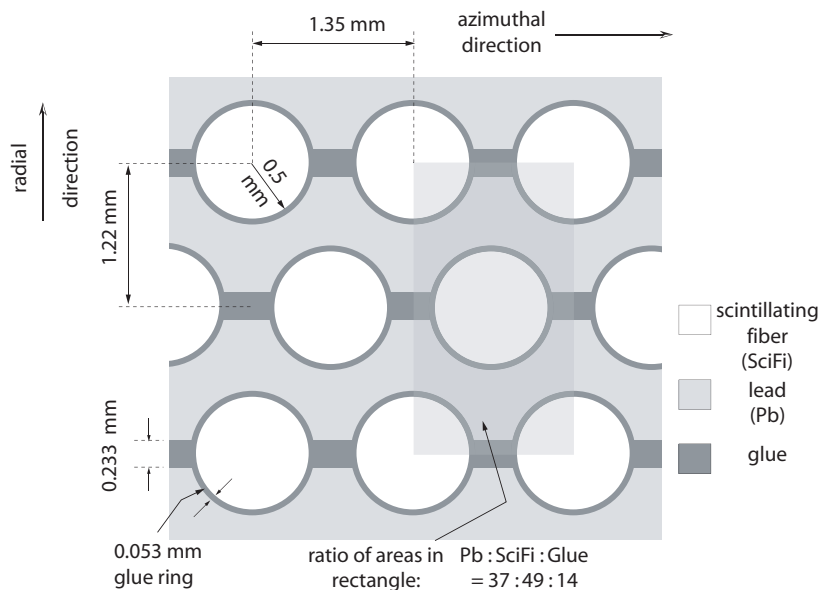

Figure 2.3: BCAL fiber matrix showing the placement of 1 mm diameter fibers in the azimuthal and radial directions. The dimensions of the azimuthal and radial pitch, the glue box between the lead sheets and the glue ring around the fibers are based on measurements of the prototype module using a microscope. The ratio of areas within the semi-opaque rectangle are Pb:SciFi:Glue = 37:49:14. The fiber area occupies 48% of the area enclosed by the semi-opaque rectangle. More details are given in [3].

Property	Symbol	Value	References
Number of modules	N_{mod}	48	
Module length	L	390 cm	
Module inner cord	c_i	8.51 cm	
Module outer cord	c_o	11.77 cm	
Module thickness	d	22.5 cm	
Module azimuthal bite	$\Delta\phi$	7.5^o	
Radial fiber pitch	p_r	1.22 mm	
Azimuthal fiber pitch	p_ϕ	1.35 mm	
Fiber diameter	d_f	1.0 mm	
First cladding thickness	t_{c1}	0.03 mm	[7]
Second cladding thickness	t_{c2}	0.01 mm	[7]
Core fiber refractive index	n_f	1.60	[7]
First cladding refractive index	n_{c1}	1.49	[7]
Second cladding refractive index	n_{c2}	1.42	[7]
Trapping efficiency	ε_f	5.3% (min) 9.3% (max)	[7, 8]
Attenuation length	λ	240 cm	[9]
Effective speed of light	v_{eff}	$\sim$16 cm/ns	
Volume ratios	Pb:SciFi:Glue	37:49:14	[3]
Effective mass number	A_{eff}	179.9	[3]
Effective atomic number	Z_{eff}	71.4	[3]
Effective density	ρ_{eff}	4.88 g/cm^3	[3]
Sampling fraction	f_s	0.125	[10]
Radiation length	X_0	7.06 g/cm^2 or 1.45 cm	[3]
Number of radiation lengths	nX_0	15.5X_0 (total thickness)	[3]
Critical energy	E_c	11.02 MeV (8.36 MeV)	[11] ([12])
Location of shower maximum	t_{max}	5.0X_0 (5.3X_0) at 1 GeV	[11] ([12])
Thickness for 95% containment	$t_{95\%}$	20.3X_0 (20.6X_0) at 1 GeV	[11] ([12])
Molière radius	R_M	17.7 g/cm^2 or 3.63 cm	[12]
Energy resolution	σ_E/E	$5\%/\sqrt{E} \oplus 1\%$	[13]
Time difference resolution (photons)	$\sigma_{\Delta t}$	$75 \text{ ps}/\sqrt{E} \oplus 30$	[13]
Mean time resolution (m.i.p's)	σ_{MT}	420 ps	[9]
z-position resolution	σ_z	$5 \text{ mm}/\sqrt{E}$ (weighted)	
Azimuthal angle resolution	σ_ϕ	~ 8.5 mrad	
Polar angle resolution	σ_θ	~ 8 mrad (at $\theta = 90^o$)	

Table 2.1: BCAL properties.

2.3 BCAL beam tests

2.3.1 Charged particle beams at TRIUMF

The first beam tests of Module 1 were performed at the TRIUMF's M11 area in June 2005, together with prototypes of the GLUEX time-of-flight (TOF) modules in collaboration with Indiana University. Figure 2.4 shows a schematic of the detector placement and readout for BCAL Module 1. Module 1 was placed with its long side perpendicular to the beam and its 23 cm side along the beam direction. Two beam momenta were used - 120 MeV/c at 18 Hz and 250 MeV/c at 22 Hz, with e^+'s, μ^+'s and π^+'s present in the beam. A z-position scan was carried out with the beam always perpendicular to the long side of the module. The incoming beam was defined by a two scintillation counters, T1 ($1 \times 1 \times 6$ cm^3), that also provided the start time for all systems, and T2 ($1 \times 1 \times 1$ cm^3) placed 15 cm before the TOF counters. The TOF counters were 1 cm thick.

Module 1 had four PMT units attached - two on each side. The light guides covered an area of 10×10 cm^2, from 1.5 cm to 11.5 cm along the 13 cm side (Figure 2.4). The light guides of the Front PMTs cover the first 10 cm of depth from the face on which the beam is incident, and the light guides of the Back PMTs cover the next 10 cm (the last 3 cm were not covered, but Monte Carlo simulations show that no more than 1% of the energy is deposited there for the particle energies used during the TRIUMF test).
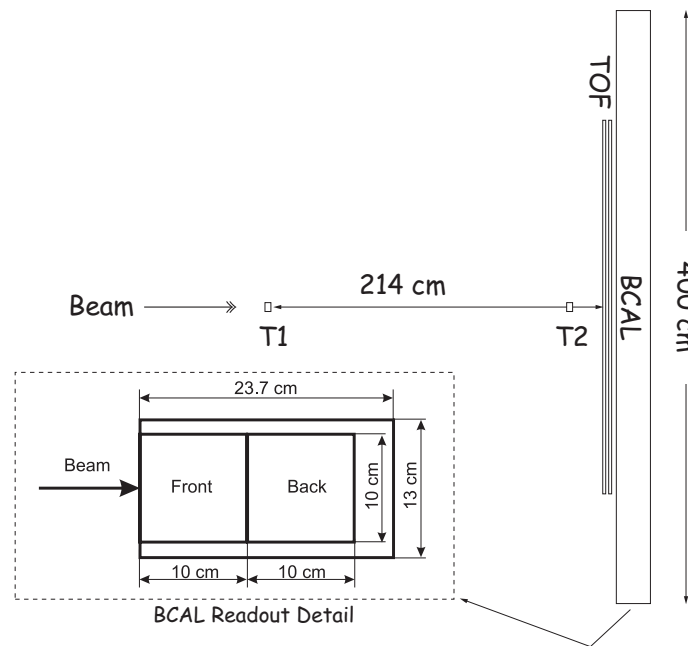

Figure 2.4: A schematic of the detector placement and readout for BCAL Module 1 for the beam tests at TRIUMF.

The TRIUMF beam tests provided the first opportunity to use beam data to validate the GEANT-based simulations of the full-scale prototype. The data were also used to obtain information about energy resolution, mean time resolution, effective speed of light in the scintillating fibers and the attenuation length of the fibers. Details are presented in the M. Sc. thesis of G. Koleva [14].

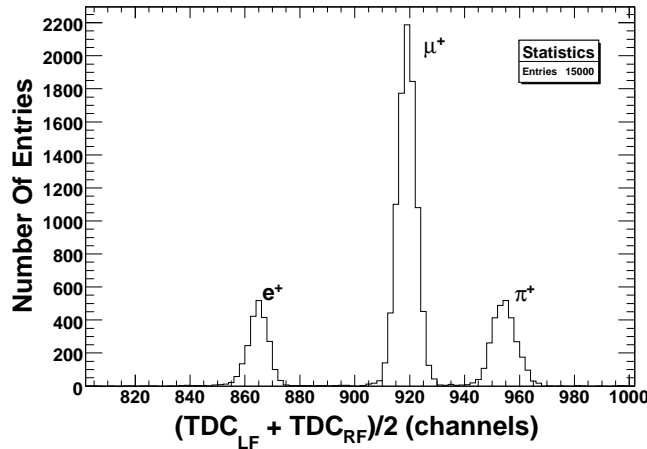Figure 2.5 shows the mean time in TDC counts of the arrival time as measured by the left front (LF)

Figure 2.5: Mean of the arrival times (in TDC) counts measured by the left front (LF) and right front (RF) PMT's for 120 MeV/c beam.

and right front (RF) PMT's for 120 MeV/c beam. This shows clear peaks for e^+'s, μ^+'s and π^+'s. The effective speed of light in the scintillating fibers was measured by measuring the left-right time difference as a function of position along the module using 120 MeV/c positrons. This yielded $v_{eff} = 16.2 \pm 0.4$ cm/ns. The attenuation length of the fibers was determined to be 307 ± 12 cm. A direct measure of the energy resolution dependence on energy at the two beam momenta was obtained by determining the width σ of the distribution in the geometric mean of the ADC's from the left and right PMT's divided by the mean μ of that distribution. The geometric mean is computed as $ADC_{GM} = \sqrt{ADC_L \cdot ADC_R}$. The geometric mean removes the effect of finite attenuation length of the fibers as the beam moves away from the center of the module. It was found that $\sigma/\mu = (24.6 \pm 0.3)\%$ for 120 MeV/c positrons and $\sigma/\mu = (16.9 \pm 0.2)\%$ for 250 MeV/c positrons.

2.3.2   Photon beams at JLab

Module 1 was also tested in a photon beam at JLab by placing the module in the alcove at the downstream end of Hall B. Figure 2.6 shows a schematic of the alcove area, the platform in front of the alcove and the possible positions for Module 1 with its readout.

Bremsstrahlung photon beam: The bremsstrahlung photon beam in Hall B provided a spectrum of photons from 150 MeV up to 650 MeV produced by the 675 MeV electron beam from CEBAF incident on a radiator. The electron beam current was 1 nA. The scattered electrons were tagged and provide timing and momentum information for the photons. The tagger provides the momentum information from 384 individual scintillator paddles, called E-counters, with a photo-tube on each end. They are arranged so that they each cover constant momentum intervals of $0.003E_0$. Each counter optically overlaps its adjacent neighbour by 1/3 creating 767 individual photon energy bins providing an energy resolution of $0.001E_0$. The timing information is provided by 61 individual scintillator blocks, called T-counters, with phototubes attached at both ends. The T-counters are in two groups. The first 19 narrower counters cover 75% to 90% of the incident electron energy range and the remaining 42 counters cover the 20% to 75% range [15]. The trigger is formed from the Master OR from the tagger of the T-counters and an OR signal from the North

and South of the BCAL module. On average, the event rate was around 1 to 4 kHz for the duration of the beam test. The beam was collimated with a 2.6mm collimator giving a beam spot size on the BCAL module of 2cm in diameter.
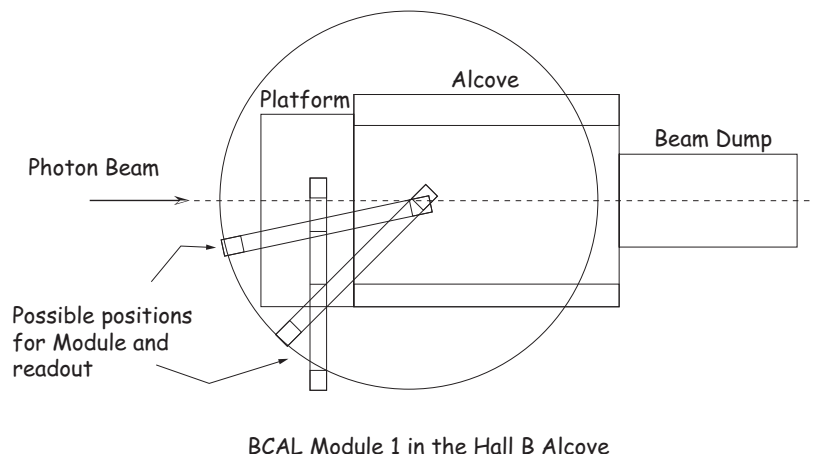

BCAL Module 1 in the Hall B Alcove

Figure 2.6: A schematic of the detector placement for the BCAL Module 1 beam tests in Hall B at Jefferson Lab.

Readout and electronics: Each end of the module was segmented into 18 cells, each 3.81×3.81 cm^2 in area, as shown in Figure 2.7. Square light guides with a 45 degree mirrored surface channelled the light from the scintillating fibers to PMTs on the South and North ends. Silicon sheets, approximately 2.5 mm thick, were used to interface the light guides with the module and circular cookies to couple the light guides to the PMTs. Everything was then enclosed in a steel box. The light boxes and PMT's can be seen in the photo of Figure 2.8. The first three rows are read out using XP2020 photomultiplier tubes because of their better timing characteristics and since most of the energy is deposited in the first 12 cm of the BCAL. The last three rows are read out using Burle 8575 tubes. Data runs were taken with the photon incident at various angles and positions along the module by translating and moving the module. More details about the run setup can be found in reference [13].

Two cosmic ray scintillation counters (paddles) were used for the beam tests. The two cosmic ray paddles were each 10×40 cm^2 and were oriented with their long side perpendicular to the BCAL module. One paddle was located ≈ 2.5 cm above the top sector and the other was located ≈ 7.5 cm below the bottom sector of the BCAL module. The mid-point of the long dimension of the paddles was located between layers 3 and 4 of the BCAL module (please refer to Figure 2.7).

Calibration and energy resolution: Initial gain equalization among the module PMT's was performed using cosmic ray triggers before data taking with the photon beam. For photon running, an overall calibration constant, that converts ADC counts to energy, was determined by requiring the distribution of the geometric mean of the North ADC sum and South ADC sum, divided by beam energy, to be centered at unity. Inter-segment calibration was performed in two ways, one method using photon data with the beam at the center of the module at normal incidence, and the other method using cosmic ray data. Using photon data [13], the calibration constants for individual PMT's were varied to minimize the width of the distribution of $E_{CAL} - E_{beam}$ where E_{CAL} is the calorimeter energy based on the geometric mean of the North and South ADC sums and E_{Beam} is the beam energy reported by the tagger. Using cosmic ray data [16], events were
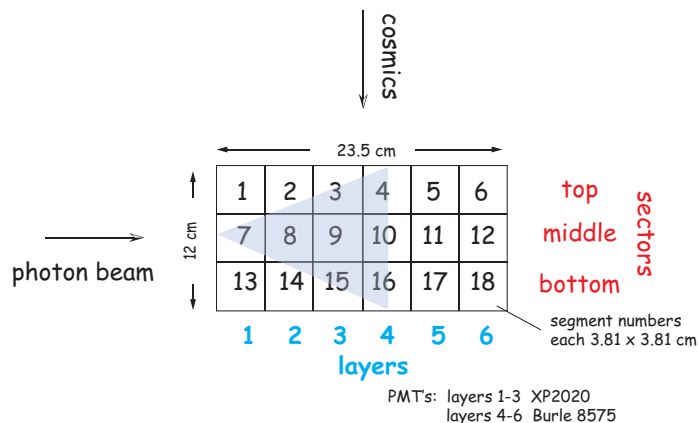
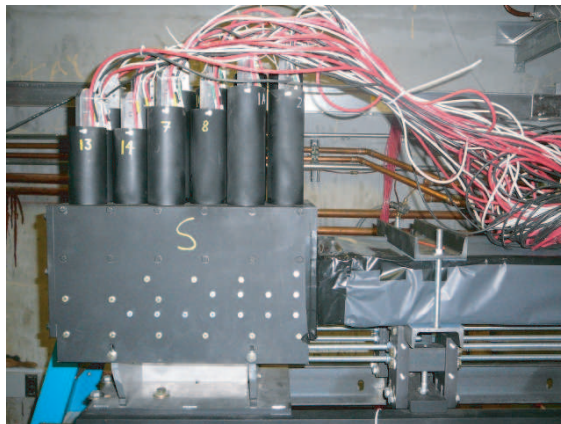Figure 2.7: Readout segmentation for one end of the BCAL module showing segment, layer and sector naming.

Figure 2.8: The black box encloses the 18 light guides and PMTs with cables attached for the South end of the BCAL module and is similar to the North end. The BCAL Pb/Sci-Fi matrix is wrapped in Tevlar on the right and pressed against the light guides coupled with a silicone cookie.

selected for which a through-going minimum ionizing particle was confined within a layer. Constants were then tuned to give equal responses among all PMT's. The two methods yielded consistent results.

The energy resolution as a function of energy was parameterized as:

$$\frac{\sigma_E}{E} = \frac{a}{\sqrt{E(\text{GeV})}} \oplus b \tag{2.1}$$

where the two terms are added in quadrature. For various bins in $E = E_{beam}$, the distribution in $|E_{CAL} - E_{beam}|/E_{beam}$ is fitted to a Gaussian to obtain σ_E. The dependence of σ_E/E on E is shown in Figure 2.9(a), for normal incidence at the center of the module, using calibration constants derived from cosmic ray data (the fit to equation 2.1 yields $a = 0.056 \pm 0.001$ and $b = 0.029 \pm 0.001$) and calibration constants using the minimization technique ($a = 0.056 \pm 0.001$ and $b = 0.020 \pm 0.001$). This resolution is consistent with that obtained by KLOE. In our case leakage out the sides contributes 2% to the floor term (equation 2.1). The

terms a and b are independent of position along the module but they do depend on the angle of incidence as shown in Figure 2.9(b) where the dependence of a and b on angle of incidence is shown. Recall, from the discussions above, that for GLUEX reactions, most of the photons strike BCAL with angles less than 40°. The degradation in the floor term is due to part of the electromagnetic shower escaping detection out of the front of the detector. The improvement in the floor term going from normal incidence to 90° is due to improved shower containment since at this angle the photon trajectory penetrates 25 radiation lengths of the Pb/SciFi matrix compared to 15.5 radiation lengths at normal incidence.
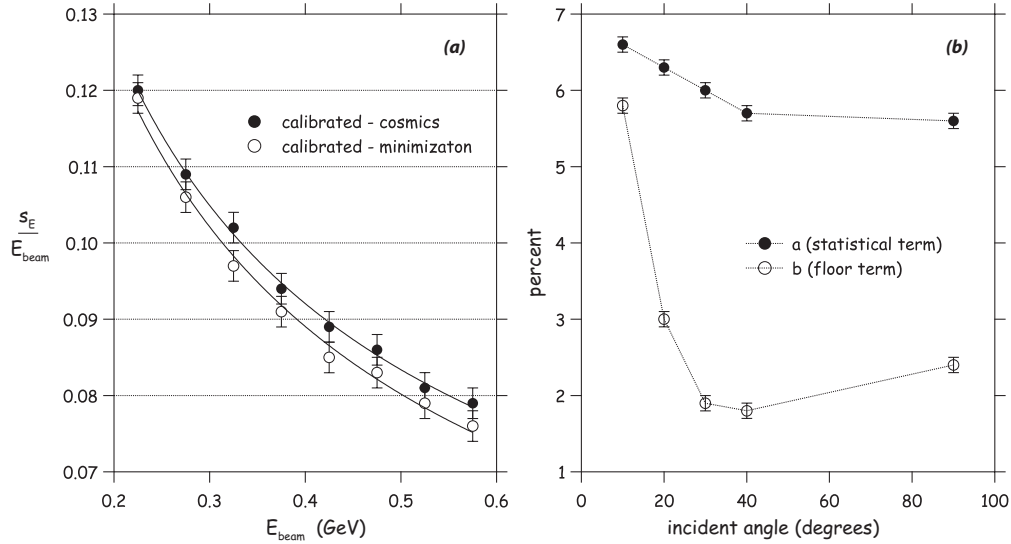

Figure 2.9: (a) σ_E/E as a function of E for calibration constants derived using the minimization technique and derived from analysis of cosmic rays. The fits are to the function of equation (2.1); (b) the variation of a and b with incident photon angle.

Time difference resolution: As pointed out in Section 1, the time difference between the ends of the module measures the position of the photon along the module and is critical in determining the four-vector of the photon. Because leading edge discriminators were used, the timing had a dependence on pulse height which required a time walk correction. Timing data were analyzed for the run with the photon beam normally incident at the center of the module. Plots of TDC versus ADC for segments 7, 8 and 9 (those with the most energy) were fit to a function of the form $p_0/\sqrt{ADC} + p_1$ ns. The time delay due to signal amplitude in leading edge discriminators is expected to have this dependence. The p_1 term is the timing offset of the particular BCAL cell from the tagger timing signal with a value of approximately 530 ns. The parameter p_0 has a nominal value of 30 ns·$\sqrt{ADC}$ to 40 ns·$\sqrt{ADC}$. This functional form is then used to do the time walk correction.

Figure 2.10 is the time difference resolution as a function of beam energy. The time difference resolution is obtained by fitting the distribution in $\Delta t = t_S - t_N$, the North-South time difference, to a Gaussian for bins of beam energy. A fit to a function of the form:

$$\sigma_{\Delta t} = \left(\frac{c}{\sqrt{E(\text{GeV})}} \oplus d \right) \text{ ps} \tag{2.2}$$

In the appropriate units, $c = 74.9 \pm 0.4$ and $d = 30.0 \pm 2.7$. The constant term is a result of some residual calorimeter miscalibrations, but some of it is also due to the finite width, $\Delta z = 1.8$ cm, of the beam which will contribute, in quadrature, to the time difference by $(\Delta z/\sqrt{12})/v_{eff} = 28$ ps. We note here that for the KLOE calorimeter, $\sigma_{\Delta t} = (56/\sqrt{E(\text{GeV})} \oplus 133)$ ps.
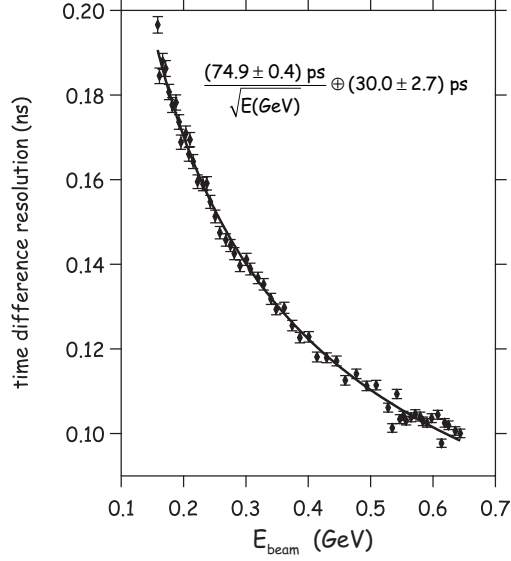

Figure 2.10: The time difference resolution as a function of beam energy. The time difference resolution is obtained by fitting the distribution in $\Delta t = t_S - t_N$, the North-South time difference, to a Gaussian for bins of beam energy.

Mean time resolution: The mean time, $\bar{t} = (t_N + t_S)/2$, provides information on the arrival time of the photon. It also provides time of flight information for charged particles: $\pi^\pm, K^\pm, p$. Photons, protons and minimum ionizing particles are characterized by very different patterns of energy loss and will therefore have very different resolutions for $\bar{t}$. From the beam test data, the resolution in $\bar{t}$, $\sigma_{\bar{t}}$, for photons has the same dependence on energy as given by equation 2.2 with $\sigma_{\bar{t}} = (34/\sqrt{E\text{GeV}} \oplus 210)$ ps.

To estimate $\sigma_{\bar{t}}$ for minimum ionizing particles, cosmic ray data were used [9] and the result is that for minimum ionizing particles, $\sigma_{\bar{t}} = 420$ ps. The implication of this result is that BCAL can be used to for π/p separation but not for π/K separation. More details on extracting the mean time resolution from cosmic rays are given in reference [9].

Estimating the number of photoelectrons for photons: The number of photoelectrons (N_{pe}) per end of the prototype BCAL module was estimated using data with the photon beam normally incident at the center of the module. For each of eight bins in beam energy, from 200 to 600 MeV, the distribution in the ratio of the north sum to the south sum was fitted to a Gaussian, yielding μ_R and σ_R. Using the ratio instead of the individual summed energies cancels out the effect of shower fluctuations. Under the assumption that N_{pe} is given by:

$$N_{pe} = 2\frac{\mu_r^2}{\sigma_R^2} \tag{2.3}$$

the photoelectron yield per end is plotted in Figure 2.11 as a function of beam energy. A fit to a straight line:

$$N_{pe} = \alpha + \beta \cdot \mathrm{E(MeV)} \tag{2.4}$$

yields $\alpha = 14 \pm 4$ and $\beta = 0.634 \pm 0.01$. Extrapolating to 1 GeV yields $N_{pe} = 647 \pm 10$.
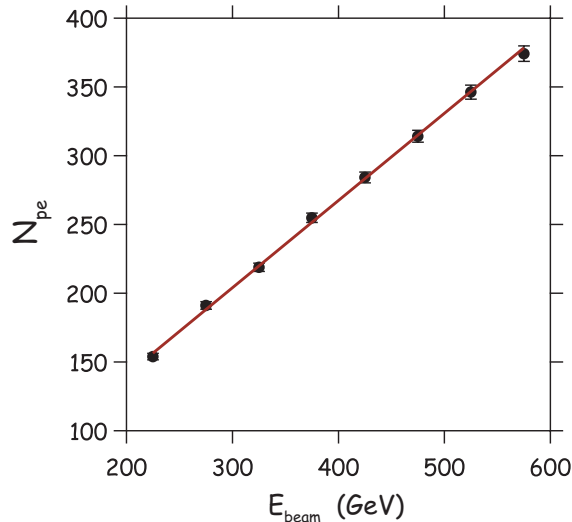

Figure 2.11: The number of photoelectrons per end of the BCAL module as a function of energy.

For the highest energy point (575 MeV) in Figure 2.11, the number of photoelectrons is 374 ± 6. Another approach is to apply the technique to each of the 18 segments of the BCAL module to get a number of photoelectrons per segment and then sum. The total number of photoelectrons in the 6 segments in the center of the module (segment 7 through 12) is 373 ± 7. Summed over all segments $N_{pe} = 440 \pm 8$. Applying the scaling factor of $440/374 = 1.18$ to the 647 ± 10 photoelectrons at 1 GeV found above yields $N_{pe} = 761 \pm 12$ at 1 GeV. So we estimate N_{pe} to be between 650 and 750. In comparison, KLOE reported $N_{pe} \sim 700$ per end at 1 GeV (see Appendix A below). For the KLOE calorimeter, a 1 GeV photon yielded a total ~ 1400 photoelectrons contributing 2.7% to the overall energy resolution of 5.4% (see Appendix A).

The KLOE calorimeter used single-clad fibers whereas the BCAL prototype used double clad fibers. The fraction of light captured within the fiber should improve by a factor of ~ 1.6 using double-clad fibers but the light guide used in the beam test had a net transmission efficiency that was likely lower than what was achieved by KLOE by a factor ~ 1.6. The issue of N_{pe} will be revisited below where the use of green emitting SciFi with SiPM is discussed.

Estimating the number of photoelectrons for minimum ionizing particles: An analysis of four cosmic ray data runs was carried out to estimate the N_{pe} per module segment for minimum ionizing particles [6]. The four runs had the cosmic ray trigger paddles located at different positions along the module, at $+150$ cm, $+100$ cm, -50 cm and -150 cm from the center of the module. Referring to Figure 2.7, to select the pedestals in a given segment in a layer, we require a low ADC count (< 10) in the two remaining segments of the layer of interest as well as in all segments of the neighboring layers. To select a cosmic ray, *i.e.* minimum

ionizing particle, in a segment, we require a large ADC counts (> 70) in each of the two segments in that layer and small ADC counts (< 10) in all the segments of the neighboring layers. The pedestal subtracted amplitude spectra for both North and South PMT's associated with each of the segments were described as a convolution of the Poisson distribution (that represents the photoelectron statistical fluctuation) and the Gaussian functions (that represents PMT gain resolution and the pedestal contribution).

The widths of the observed spectra are the result of both the fluctuations in the number of photoelectrons (North-South uncorrelated effect) and the variations in the energy deposited in the calorimeter segment (North-South correlated effect). To address this extra-broadening of the spectra, the energy deposition from the muons was simulated using the FLUKA 2006.3b program. In the simulation, the primary muon polar angles were seeded according to the $\cos^2 \theta$ distribution expected for cosmic rays, the azimuth angles as well as the coordinates of the emitting points (in the top trigger paddle limits) were seeded uniformly, and (to meet the trigger conditions) the hits of the bottom trigger paddle were required. The simulated Birks-corrected energy depositions in the fibers summed over each of the calorimeter segment were recorded on event-by-event basis, and the cosmic ray selection cuts were applied.

The mean number of photoelectrons ($N_{pe}^{mean} \equiv \sqrt{N_{pe}^{North} \cdot N_{pe}^{South}}$), averaged over all segments and all runs, is 25.5±0.7. The observed strong linear correlation between mean amplitudes (averaged on run-by-run basis) and correspondent extracted mean numbers of photoelectrons indicates that the technique does reliably extract the number of photoelectrons.

The N_{pe} was also estimated by fitting the North/South ratio spectra for each of the 18 segments. Averaged over all segments and all runs, $N_{pe} = 22.0 \pm 0.9$. KLOE studies [17] of blue fibers coupled directly to a bi-alkali photocathode 2 m from a crossing minimum ionizing particle yields about $N_{pe} - 1.7$ to $N_{pe} - 2.3$ per mm of traversed fiber. The BCAL module segment corresponds to ~ 19 mm of traversed fiber or $N_{pe} \sim 38$. The lower number obtained with the BCAL module is consistent with the expected transmission through the light guides with the mirrored-surface prisms.

As a by-product of this analysis the attenuation lengths of the fibers was measured for the single-ended analysis and the ratio analysis to yield $\lambda = 229.1 \pm 2.5$ cm and $\lambda = 235.4 \pm 1.7$ cm respectively. These results differ from the results obtained in the TRIUMF tests because inclusion of particles whose ionization is larger than minimum ionizing tends to increase the measured value of λ. The trigger used in the TRIUMF tests was loose enough to include showering particles.

Reconciling photon data results with cosmic ray results: For contained cosmic rays in a single layer, referring to Figure 2.7, the summed ADC distribution peaks at 1007 channels. A layer consists of a vertical stack of three segments. From photon beam data, the overall conversion of ADC counts to energy 0.107, that is, energy = 0.107× ADC counts. So a vertical penetrating cosmic ray is equivalent to a photon horizontally incident with energy 107 MeV. Based on the above N_{pe} yield estimates, we expect $N_{pe} \sim 75$ for three segments. A 107 MeV photon should yield $N_{pe} \sim 75$ per end. Extrapolating this to 1 GeV corresponds to ~ 715 photoelectrons, consistent with the N_{pe} estimates from photon data.

A vertically incident cosmic ray passes through 3 segments. Each channel is 38.1 mm thick and on average corresponds to 19 mm of scintillating fiber. Assuming an energy loss of 2 MeV/cm in scintillator, that corresponds to 3.8 MeV per segment or 11.4 MeV for three segments. The equivalence of a vertically passing cosmic ray to a 107 MeV photon corresponds to a sampling fraction of about 11%, assuming more or less full shower containment for the photon.

2.4 BCAL readout

2.4.1 Readout segmentation

Monte Carlo simulations of electromagnetic showers and their reconstruction indicate that the early part of the shower development is critical in achieving the required energy and directional resolution [18]. These studies also show that the inner region of BCAL, corresponding to about one-half of module thickness, should have 24 readout segments, per module end, of approximately equal area, 4 along the azimuth and 6 in depth. Each segment is approximately 2×2 cm^2 in area[1]. The task for the outer region is to measure remaining energy deposition but the requirements on segmentation are more relaxed. Studies show that 4 segments, 2 along the azimuth and 2 along the radius (depth) suffice. We also note that in GLUEX, the bulk of the photons hitting BCAL are incident at small angles measured with respect to the module surface. A substantial fraction of photon trajectories will traverse a length of the BCAL matrix corresponding to more that 1.5 to 2 times the module thickness of 15.5 radiation lengths. To summarize, BCAL requires a total of 2304 readout segments for the inner region and 384 for the outer region. This "division of labor" between the inner and other regions of BCAL meets the physics requirements while at the same time minimizing readout channels, and therefore costs. It allows us to consider using different technologies to readout the two regions.

2.4.2 Photosensor options

The nominal central field of the GLUEX solenoid is 2.2 T and the field in the region at the ends of the BCAL module is substantial with large gradients [19] so using vacuum PMT's with short light guides is not possible. One option is to use vacuum PMT's and to transport the scintillation light via rigid light guides, liquid light guides or fibers out to a region outside the solenoid where the field is sufficiently small that PMT shielding could be employed. Another option is to use silicon photomultipliers (SiPM), which are immune to large magnetic fields, with compact light guides.

Using the first option for the inner region, with over 1100 channels per BCAL end, would require using clear fiber optic guides as opposed to rigid guides. But even accommodating 1150 fiber bundles out of each end of BCAL, within the physical space constraints, is a challenge. Another significant issue is cost. It is essential to maintain high light collection efficiency to meet energy and timing resolution requirements. The fiber characteristics would have to be well-matched to those of the scintillating fibers and have high transport efficiency. For the outer region, with an order of magnitude fewer readout channels and somewhat more relaxed requirements with regard to transport efficiency, rigid light guides or fibers are a viable option and are being considered for used for BCAL [20, 21, 22].

The second option of using SiPM with compact light guides, despite some technical challenges, has been selected as the readout option for the inner region. SiPM based photo-sensors are compact, they do not require high voltage supplies and cables, they have good gain and excellent dynamic range. They are immune up to at least 5 T fields. These characteristics also lead to an optimization of the coupling of the sensors to BCAL directly using a Winston cone. Such an assembly exhibits light transmission efficiencies unmatched by any other light transport system to the photo-sensors. The major problem is that they are commercially available only in small sizes, typically of 1.0×1.0 mm^2, 2.0×2.0 mm^2 and only very recently 3.0×3.0 mm^2.

---

[1]We note that the readout segment for KLOE was 4.4×4.4 cm^2 in area. The inner radius of the KLOE calorimeter was 2 m compared to 0.65 m for BCAL

Considering that the inner layer read-out cell size is approximately 2.0×2.0 cm^2, this option faces the technical challenge of developing a larger area SiPM that still satisfies the requirements on timing and energy resolution of GLUEX. The group from the University of Regina has been working with engineers at SensL[2] to develop and test such large area SiPM arrays, using 4×4 cells, each 3.0×3.0 mm^2 in area, for use in GLUEX [23, 24, 25, 26, 27, 28, 29, 30, 31, 32]. Five prototypes have been tested against our experimental requirements. The primary issues that need to be addressed include gain uniformity across the array and time structure of the output pulses, while maintaining all other qualities of the photon sensor, such as low dark current. We expect these issues to be resolved during the next development phase. Section 3 of this Report covers the status of SiPM development and measurements for application with BCAL.

2.4.3 Scintillating fiber/photosensor matching

The KLOE detector used blue scintillating fibers coupled to bi-alkali PMTs. BCAL Module 1 used also used blue scintillating fibers coupled to bi-alkali PMTs, the main difference being the use of double-clad fibers for BCAL as opposed to single-clad for KLOE. The fraction of light captured for double-cladding to single-cladding is in the ratio 5:3. As argued above, the optimal photosensor for the inner portion of BCAL is the SiPM. Figure 2.12(a) shows the quantum efficiency of the Amperex XP2020 (used in the BCAL photon beam tests) and Figure 2.12(b) shows the photon detection efficiency of the SensL silicon photomultiplier A35H over the range of relevant wavelengths. As will be shown below, the emission spectrum of blue-emitting scintillating fibers are well matched to the bi-alkali PMT but a green-emitting fiber is a better match to the SiPM.
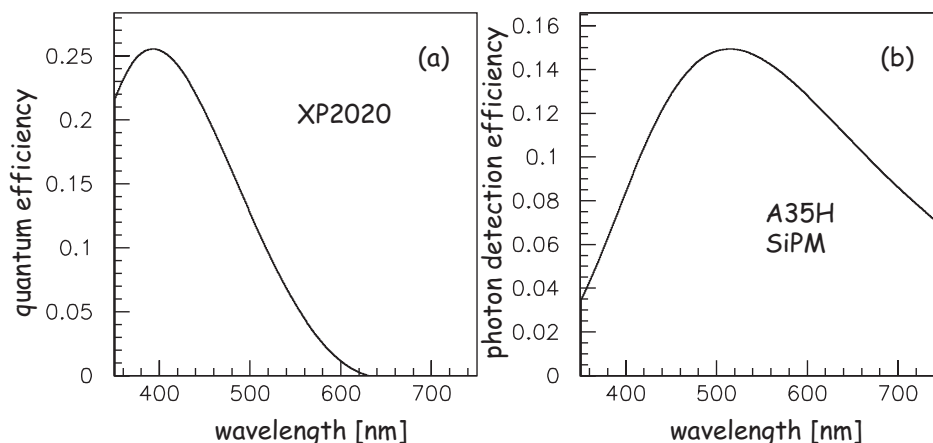

Figure 2.12: The photon detection efficiency over the range of relevant wavelengths for the (a) Amperex XP2020 and the (b) SensL silicon photomultiplier A35H at +2V above breakdown voltage.

The University of Regina group made measurements of the emission spectra of PolHiTech and BCF-20 scintillating fibers using a spectrophotometer. One end of a fiber terminated at the spectrophotometer[3] aperture while the distance d of the excitation source (light from a 380 nm UV LED) from the spectrophotometer end was varied from $d = 8$ cm to $d = 390$ cm. The emission spectra at the source ($d = 0$ cm) for the PolHiTech fiber was assumed to follow the emission spectrum for BCF-12[4]. Footnote 4 also shows the emission spectrum, at the source, for BCF-20. The emission spectra at the source ($d = 0$) and from $d = 8$ cm to

---

[2]See – www.sensl.com.

[3]Ocean Optics Fiber Optic spectrophotometer SD200 - see http://www.oceanoptics.com/products/s2000.asp

[4]Saint-Gobain scintillating fiber brochure posted as GlueX-doc-917.

$d = 390$ cm are very well described by either a single Moyal function or a sum of two Moyal functions. The Moyal function is often used to approximate a Landau distribution and is defined as:

$$f(x, \mu, \sigma) = \exp\left(-\frac{1}{2}\left(\frac{(x - \mu)}{\sigma} + e^{-(x-\mu)/\sigma}\right)\right) \tag{2.5}$$

Figure 2.13 shows the fitted spectra for the PolHiTech and BCF-20 fibers. The source spectra (filled yellow) were normalized to match the 8 cm measured spectra at 550 nm for the BCF-20 fiber and at 520 nm for the PolHiTech fiber.

For the blue-emitting fiber there is a significant loss of light in going from the source ($d = 0$ cm) to $d = 8$ cm as can be seen by comparing the areas under the two emission spectra. The emitted light is absorbed within a short distance for the smaller wavelengths. The corresponding light loss for the green-emitting fiber is far less severe.
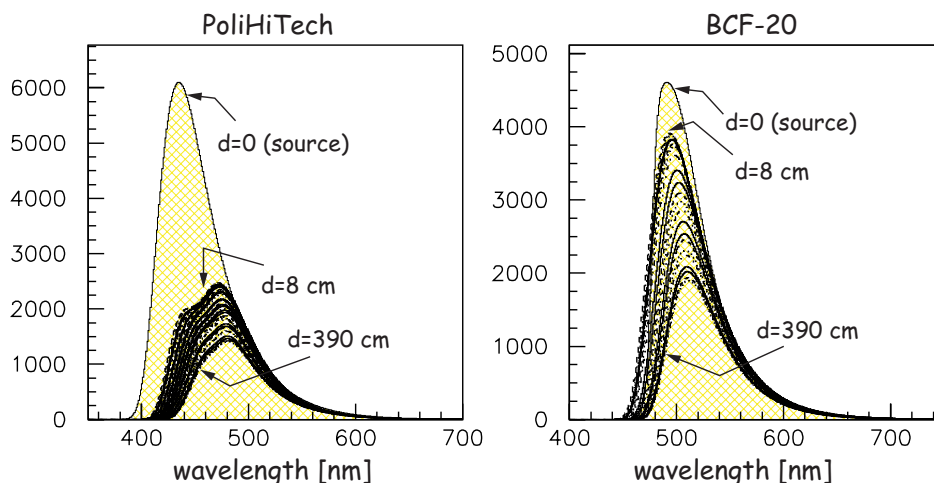

Figure 2.13: The Moyal representations of the source and measured spectra for the PolHiTech and BCF-20 fibers. The source spectra (filled yellow) were normalized to match the 8 cm measured spectra at 550 nm for the BCF-20 fiber and at 520 nm for the PolHiTech fiber.

Figure 2.14(a) shows the integrated spectrum over wavelength as a function of distance from the source for the PolHiTech fiber before (filled circles) and after (open circles) convoluting with the photon detection efficiency of the XP2020. Figure 2.14(b) shows similar plots for the BCF-20 fiber. For the PolHiTech fiber, the XP2020 quantum efficiency is convoluted with the integrated spectrum at various distances from the source and for the BCF-20 fiber the photosensor is the A35H SiPM. The fits shown are double exponentials with two attenuation lengths (short and long), which are also shown in the figure. Note that for the PolHiTech fiber with the XP2020, the fraction of integrated intensity at the source seen at 200 cm from the source, folding in the quantum efficiency, is 24% while the corresponding fraction for the BCF-20 with the A35H is 61%. More details about the analysis of the emission spectra are given in reference [33].

The average quantum efficiency (QE) of the XP2020 and the average photon detection efficiency (PDE) of the A35H SiPM, where the average is that over wavelength, are computed using the emission spectra of PolHiTech (PHT) and BCF20. The integrals of these spectra over wavelength, with and without convolution with the QE (or PDE), are computed as a function of distance. The average QE (or PDE) as a function of

distance are computed by dividing the integral with convolution by the integral without convolution. The results are shown in Figure 2.15. For PolHiTech, at 200 cm from the source, the average QE of the XP2020 is 15% and that of the A35H is 14%. For BCF20, at 200 cm from the source, the average QE of the XP2020 is 9% and that of the A35H is 14%.
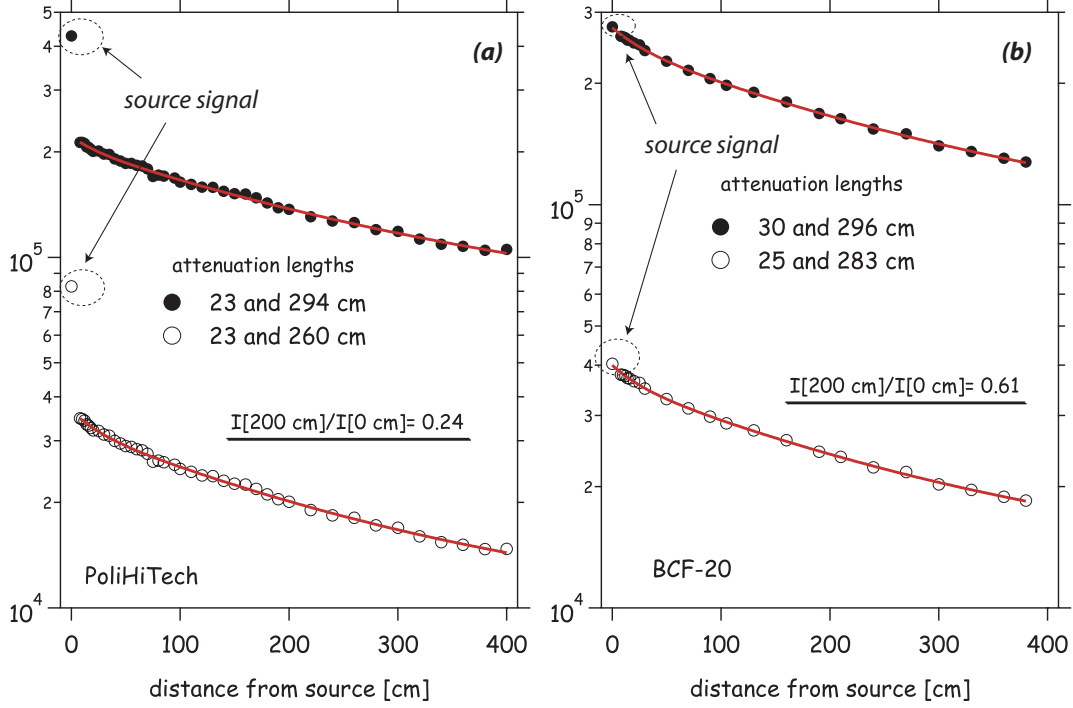

Figure 2.14: (a) Integrated spectrum as a function of distance from the source for the PolHiTech fiber before (filled circles) and after (open circles) convoluting the photon detection efficiency of the XP2020; (b) same for the BCF-20 fiber. The fits are to a double exponential with the short and long attenuation lengths quoted. The integrated signal at the source (at 0 cm) is indicated in the plots.

2.4.4   Revisiting N_{pe} estimates from cosmic rays

As discussed above, the N_{pe} yield per segment end was estimated to be $N_{pe} = 25.5 \pm 0.7$ for minimum ionizing particles passing through center of the BCAL module. We expect the photoelectron yield to be given by:

$$N_{pe} = N_0 \cdot \delta E \cdot f_{survive} \cdot f_{PDE} \cdot f_{CR} \cdot f_{trans} \qquad (2.6)$$

where:

1. N_0 is the number of photons emitted by the scintillator per MeV of deposited energy. We assume $N_0 = 8000$ photons/MeV;
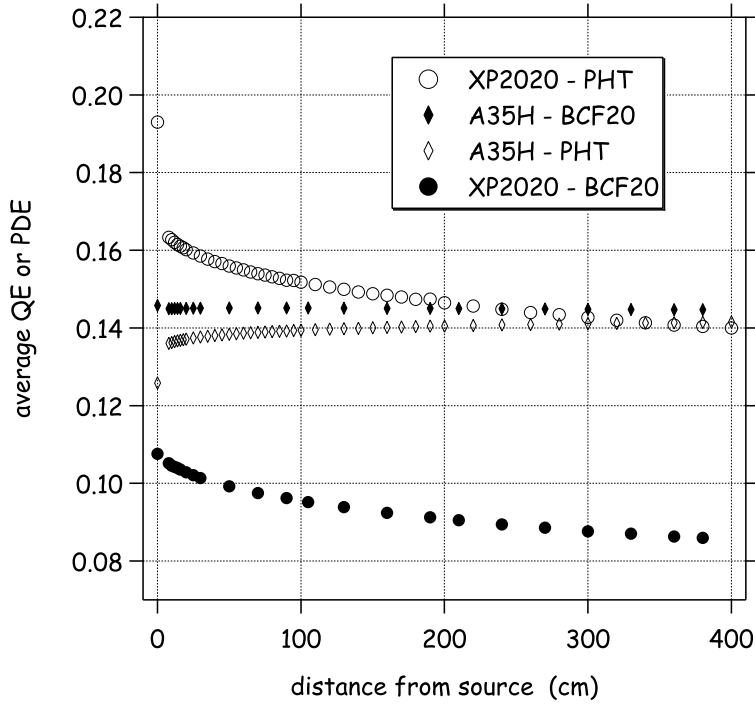
Figure 2.15: The average QE of the XP2020 and the average PDE of the A35H as a function of distance from source for PolHiTech (PHT) and BCF20 scintillating fibers. Details are given in the text.

2. δE is the energy loss for a minimum ionizing particle passing through 3.8 cm of the Pb/SciFi matrix. Using a nominal 2 MeV/cm for plastic and assuming 50% of the volume is scintillator, $\delta E = 3.8$ MeV;

3. $f_{survive}$ is the fraction of photons produced at the source that survive after 200 cm. From Figure 2.14(a) we have $f_{survive} = 0.24$;

4. f_{PDE} is the average photon detection efficiency for the XP2020 which is the average quantum efficiency (0.14 from Figure 2.15) times 0.85 (average collection efficiency) or $f_{PDE} = 0.12$;

5. f_{CR} is the capture ratio for double clad fiber. The manufacturer quotes a minimum $f_{CR} = 0.054$;

6. f_{trans} is the transmission through the light guide used for BCAL Module 1. The 45° mirrored surface was measured to have a reflectivity of $\sim 75\%$ but the overall transmission, which also includes transmission through all the interfaces and coupling to the PMT was not measured. We will assume f_{trans} between 0.5 and 0.6.

With the above assumptions we arrive at $N_{pe} = 25$ to $N_{pe} = 30$ compared to the measured $N_{pe} = 25.5 \pm 0.7$.

2.4.5 Revisiting N_{pe} estimates for a 1 GeV photon

For the BCAL module we arrived estimated $N_{pe} = 650-750$ extrapolating to a 1 GeV photon based on widths of the distributions of North/South ratios. Following the same procedure as above, we use equation 2.6 with

$\delta E = f_{sample} \cdot 1000$ MeV using a sampling fraction of 11.6% as estimated by the simulations. This results in a yield estimate $N_{pe} \approx 800$.

2.4.6 Estimating N_{pe} for green SciFi with SiPM

Compared to the KLOE, the use of green double-clad fibers, compared to blue single-clad fibers should yield a factor of four increase in the number of photoelectrons, assuming other factors (sampling fraction, f_{PDE} and f_{trans}) being equal. This is due to a factor of 2.5 increase in $f_{survive}$ (see $I(200 \ cm)/I_0$ in Figure 2.14(a) and (b)) and a factor of 1.6 increase in f_{CR} for double-clad compared to single-clad. Thus the contribution of the photoelectron statistics to the overall energy resolution should be reduced by a factor of two.

2.4.7 SiPM dark rate and energy threshold

An issue with the use of SiPM's as BCAL photosensors is the relatively high dark rate, that will have an effect on the lowest detectable energy, E_{thr}. This clearly has an impact on GLUEX physics. For example, one of the signature reactions discussed in Section 1 is the $b_1^+ \pi^0 n$ final state which results in a neutron, three charged pions and four photons. According to Figure 1.7, for 10% of the events, the lowest energy photon in the event has an energy less than 40 MeV and this fraction increases to 25% for the lowest photon energy less than 80 MeV.

In order to understand the effect of dark rate in the SiPM's, we follow the treatment presented in reference [34]. The total relative error, $\sigma(E)/E$, in the energy measurement is assumed to be due to individual contributions added in quadrature and these include (1) a constant floor term of 1%, (2) sampling fraction fluctuations; (3) photoelectron statistics; and (4) pedestal fluctuations due to dark rate. As noted above and in Appendix A below, the mean number of photoelectrons measure with the KLOE calorimeter at one end of the calorimeter for a 1 GeV photon incident at the center of the calorimeter was ~ 700 or ~ 1400 for the sum of both ends yielding an overall error photoelectron statistical contribution of 2.7%. The overall energy resolution was given by $5.4\%/\sqrt{E}$ implying a sampling fraction fluctuation contribution of:

$$\frac{\sigma_{samp}(E)}{E} = \frac{4.7\%}{\sqrt{E}} \tag{2.7}$$

The total number of photoelectrons at both ends for the calorimeter is given by $N_{pe} = N_{phot} \cdot f_{PDE}$ where N_{phot} is the total number of photons arriving at the two ends of the calorimeter. The KLOE and BCAL module yields are consistent with $N_{phot} = 11750$ if $f_{PDE} = 0.12$. The contribution to the total relative error in energy from photoelectron statistics is:

$$\frac{\sigma_{pe}(E)}{E} = \frac{1}{\sqrt{N_{phot} \cdot f_{PDE}}} \tag{2.8}$$

The contribution to the relative error due to pedestal fluctuations due to dark noise rate R_{dark} is:
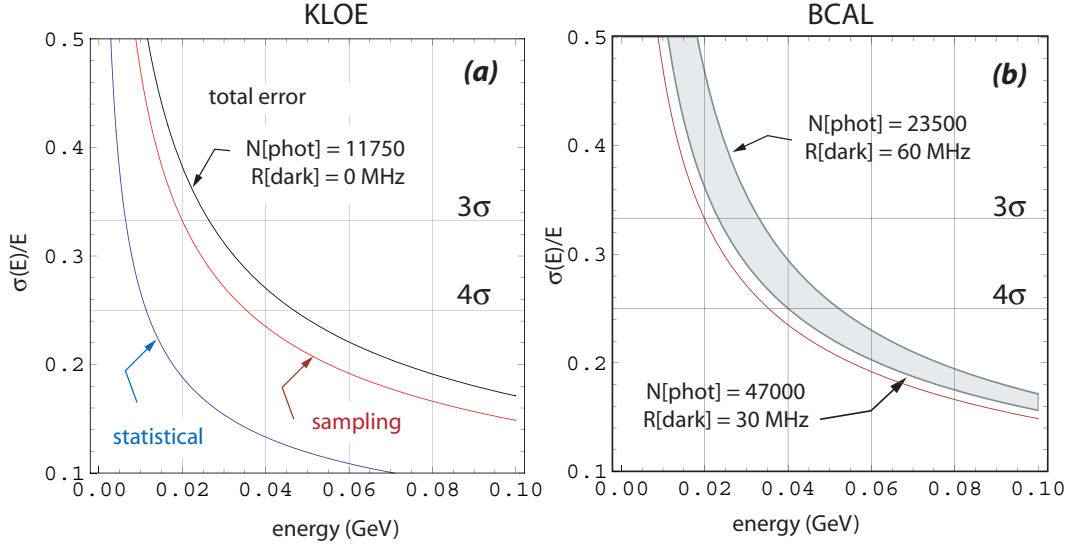
Figure 2.16: The relative error in energy measurement, $\sigma(E)/E$ as a function of energy for (a) KLOE parameters and (b) BCAL parameters. In (a) the contributions from the statistical and sampling terms are shown in blue and red. The total error includes these two terms added in quadrature along with a constant floor term of 1%. In (b) two different assumptions about photon yield and dark rate are shown. For both we assume $f_{PDE} = 0.12$. More details are given in the text.

$$\frac{\sigma_{ped}(E)}{E} = \frac{\sqrt{\Delta t_{gate} \cdot R_{dark} \cdot N_{ps}}}{N_{phot} \cdot f_{PDE}} \tag{2.9}$$

where, for BCAL, $N_{ps} = 48$ is the number of photosensors per module and $\Delta t_{gate} = 100$ ns is the gate width. In addition to this we assume a constant floor term in the energy resolution of 1%. The total error is the sum, in quadrature, of the floor term along with the contributions given in equations 2.7, 2.8 and 2.9. The quadratic sum of the fluctuations due to photoelectron statistics and pedestal fluctuations are collectively referred to as the statistical term. We show the total relative errors in Figure 2.16 for various assumptions starting with Figure 2.16(a) for the KLOE parameters where the dark rate is assumed to be negligible and $N_{phot} = 11750$ with $f_{PDE} = 0.12$. In Figure 2.16(b) we show the total error for two assumptions: (1) a four-fold increase of light over KLOE and a 30 MHz dark rate and (2) a two-fold increase of light over KLOE and a 60 MHz dark rate. Again, we assume $f_{PDE} = 0.12$.

If one applies the criteria that at the threshold energy we have $E > 4\sigma(E)$ or $\sigma(e)/E < 0.25$, then we see from Figure 2.16(b) that in one case we have $E_{thr} \approx 40$ MeV and in the other case we have $E_{thr} \approx 50$ MeV. We note that KLOE was able to reconstruct photons with energies as low as 20 MeV, but with reduced efficiency.

A The KLOE calorimeter

A.1 KLOE calorimeter construction

The KLOE calorimeter [35, 36, 37] consists of 24 lead-scintillating fiber (Pb/SciFi) modules that are 4.3 m long and 23 cm thick with a trapezoidal cross-section of bases 52.5 and 59.0 cm. The inner radius of the KLOE calorimeter is 2.0 m. The fibers run along the length of the module and are glued into grooved 0.5 mm thick lead foils. The fibers used are Kuraray SCSF-21 and PolHiTech 0046. These fibers emit "blue" light. The glue is Bicron epoxy BC-600ML [36]. The attenuation lengths of the SCSF-81 and PolHiTech fibers are 321 ± 5 cm and 284 ± 5 cm respectively [17]. The light propagation velocity in the fibers is $v_p = 16.9$ cm/ns independent of fiber type [17]. The fiber:lead:glue ratio is 48:42:10 and the matrix has an average density ρ of approximately 5 gm/cm^3 and a radiation length X_0 of approximately 1.5 cm. The sampling fraction is 12%.

A.2 KLOE calorimeter readout

There are 60 readout segments at each end of the 24 modules requiring a total of 2888 PMT's (Hamamatsu R5946/01 fine mesh 1.5-in diameter). Each segment is 4.4 cm wide and the first four layers (starting closest to the beam) are 4.4 cm thick and with the fifth layer being 5.2 cm thick. The five segments are aligned along the azimuthal angle ϕ. The segmentation for one end of a module is shown in Figure A.1.

KLOE calorimeter - readout segmentation (one end)
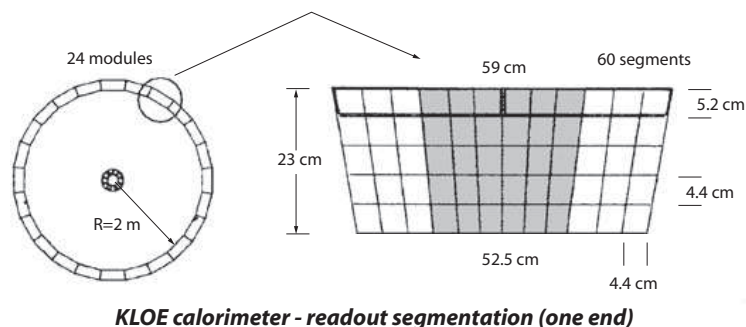
Figure A.1: Taken from Figure 5 of reference [38].

A.3 KLOE performance characteristics

The KLOE calorimeter performance characteristics [36] are summarized in Figure A.2. The energy resolution is given by $\sigma(E)/E = 5.4\%/\sqrt{E(GeV)}$ where the resolution is dominated by sampling fluctuations, the contribution from photoelectron statistics being about 2.7% at 1 GeV. This latter number was determined by looking at the fluctuation in the ratio of the response from one end relative to the other leading to an estimate of about 700 photoelectrons per side for a 1 GeV photon at the center of the module [39]. From cosmic ray tests, the photoelectron yield for 1 mm of crossed scintillator for a minimum ionizing

particle at 2 m from a "standard" bialkali photocathode PMT is $N_{p.e.} = 2.4 \pm 0.2$ for the SCSF-81 fiber and $N_{p.e.} = 1.8 \pm 0.2$ for the PolHiTech fiber [17]. The resolution in the time difference between the two ends of a module is given by $\sigma_t = 56/\sqrt{E(GeV)} \oplus 133$ ps [39]. This resolution determines the position (z) resolution along the length of the module since $\sigma_z = v_p \cdot \sigma_t/2$. The error in the transverse coordinate ($\delta(R\phi)$), where R is the inner radius) is 4.4 cm/$\sqrt{12}$. The photon detection efficiency is $> 99\%$ for $E_\gamma > 80$ MeV and the linearity is within approximately 1 to 2% for $E_\gamma > 50$ MeV [36]. The mass resolutions for the π^0 and η are completely dominated by the photon energy resolution [39]. The sigma of the diphoton mass distribution for $\pi^0 \to \gamma\gamma$ events is 14.7 ± 0.1 MeV/c^2 and for $\eta \to \gamma\gamma$ events is 41.8 ± 0.5 MeV/c^2 [40].

The major thrust of the KLOE physics program was CP and CPT studies by quantum interferometry and CP violation in K_S decays. The KLOE group also measured rare (branching ratios $\sim 10^{-4}$) radiative ϕ decays. The KLOE calorimeter was used to determine the branching ratios for $\phi \to \pi^0\pi^0\gamma \to 5\gamma$ [41] and $\phi \to a_0(980)\gamma \to \eta\pi^0\gamma \to 5\gamma$ [42].
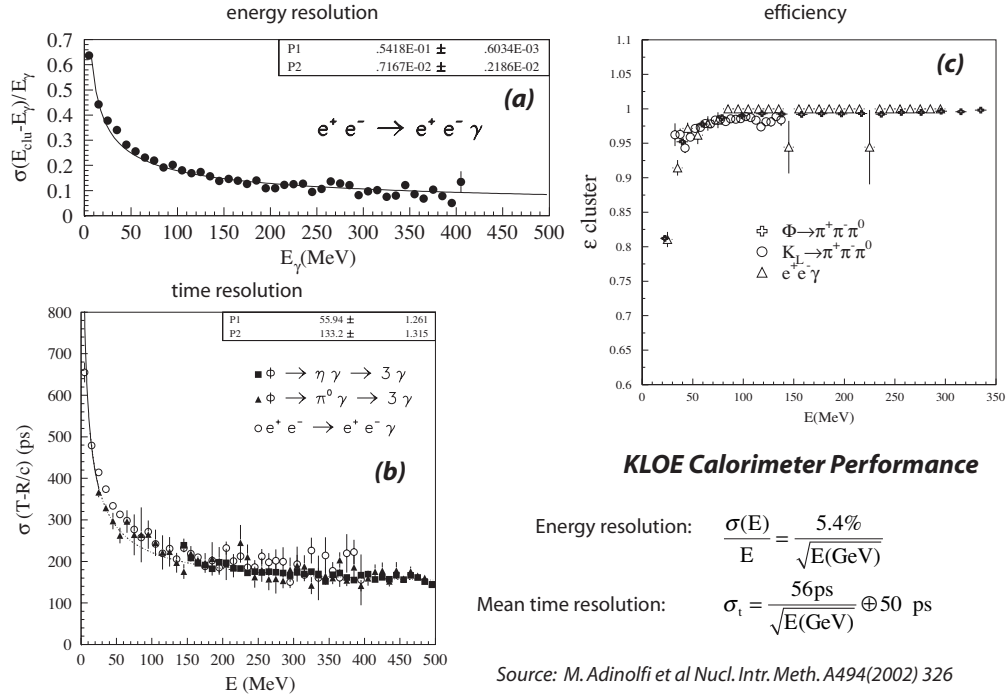

Figure A.2: Figures from reference [36]. (a) energy resolution as a function of energy; (b) time resolution as a function of energy; and (c) photon detection efficiency as a function of energy.

B BCAL module construction

B.1 Prototype module

Before constructing the first 4-m BCAL prototype (Module 1), other prototypes were constructed, much smaller in length and thickness, in order to perfect the construction techniques and to incrementally develop a technique of curing the epoxy and assuring uniform thickness. Instead of the vacuum technique used by KLOE, where the module was enclosed within a bladder and the air pumped out, thus using atmospheric pressure to apply uniform pressure, for the BCAL we decided to use electro-pneumatic pistons [43] to apply pressure. The construction techniques and the material and manpower requirements for construction have been described in a series of detailed reports [44, 45, 46], including a video documentary [47].

The first prototype (Module 0) was 2 m long with 17 cm thickness. Ten electro-pneumatic pistons, mounted on a custom designed press-frame that served as both the construction and the press/curing apparatus, were used. After completion of the Pb/SciFi/Epoxy matrix construction, machining and testing, the half-sized prototype was sent to JLab, where some tests were performed. Module 0 was a very important step because it provided the first feedback on the techniques employed, quantities of epoxy needed, manpower estimates and quality of lead required. The latter was particularly important because it established the need for pure lead of uniform thickness, a demand not easily met in North America. The use of lead-copper alloy, even at less than 1% copper content, resulted in curved sheets of the lead after swaging because the alloy was not uniform in density and patches of copper could be easily identified by eye alone. The use of pure lead of 0.5 cm thickness resulted in straight strips after swaging with less than 2% rejection rate due to curvature as they came out of the swaging machine. The swaging for Module-0 was done using a prototype machine we obtained on loan for two years from the KLOE group who also trained members of the University of Regina group on its use. A new and greatly improved swaging machine was also designed and constructed as a result of the experience gained constructing Module 0. The generosity of and help from the KLOE group was invaluable.

Based on the experience of Module 0, a new press-frame was designed and built incorporating 20 pistons along its length at 20 cm intervals. The press-frame can accommodate construction of modules up to 450 cm long with the simple addition of extra pistons. All the pistons are fed by the same high pressure air reservoir assuring equal pressure applied on a 1.25 cm thick and 410 cm long aluminum plate that distributes the pressure evenly on the surface of the module under construction during the eight hour curing phase. The pistons apply pressure equivalent to one atmosphere, thus duplicating the vacuum technique, however, the pressure is applied in timed intervals from the center toward the edges, instead of equal pressure at the same time across the module. With this technique, the epoxy that is still able to flow, flows along the length and exits at the ends, thus avoiding the *ski jump* problem that KLOE faced.

Module 1, consists of alternating layers of thin (0.5 mm) lead sheets and 1-mm-diameter, dual-clad, scintillating fibers (SciFi) from PolHiTech (0044) with peak emission wavelength of 425 nm. The lead sheets were plastically deformed after passing through a swaging machine. The fibers were glued manually in the resulting grooves with an optical BC600 epoxy, with 28:100 weight ratio of hardener to epoxy ratio. The resulting matrix (see Figure 2.3) has a fiber pitch of 1.35 mm in the horizontal direction and 1.22 mm in the vertical. The dimensions of Module 1 are: $13 \times 23 \times 400$ cm^3 (width $\times$ thickness $\times$ length). The choice of this two-part epoxy is based on the good bonding to plastic scintillator without any adverse chemical effects and it has also been proven in the construction of the KLOE calorimeter. Only the two read-out ends of Module 1 were machined and polished. Module 1 was used in the beam tests discussed below, after which it was subjected to delamination testing that it failed.

A second full-size module (Module 2) was constructed using the same techniques described above but with several significant differences. The SciFi's used were of two different types. One part (*inner*), of 13.5 cm thickness, used a new fast decay time and green emitting double-clad SciFi supplied by Saint-Gobain Crystals (formerly BICRON) type BCF-20 with peak emission wavelength of 495 nm. The other part (*outer*), of 5.5 cm thickness, consisted of the same Pol.Hi.Tech. (0044) fibers as Module 1. This hybrid design allows a testing of the performance of both types of fibers coupled to both standard vacuum-type PMT's (sensitive to either blue or green wavelengths) and to the experimental solid state photo-sensors (SiPM) under development. In addition, while Module 1 was constructed with 202 layers of Pb, each of width of 12 cm with 96 fibers each, Module 2 was constructed as a *step pyramid* starting with 12 cm width at the base and narrowing down to 8.5 cm at the top, each step being 1.2 cm high. The *step pyramid* construction, compared to rectangular construction, minimizes waste of lead and fiber when the long sides of the module are machine tapered for final assembly. Considerable effort went into the setup of clean room at the University of Alberta, where the fiber de-static process, glue mixing and gluing went on, for Modules 1 and 2.

B.2 BCAL construction issues

B.2.1 Surface preparation and delamination

As noted above, Module 1 failed the delamination test. The technique of using petroleum jelly to prevent epoxy migration to the top Pb sheet during construction and curing works very well without any loss of a module due to epoxy migration. However, the same reasons that make petroleum jelly so effective in filling up the grooves at the edges of the top Pb sheet and preventing epoxy migration, and, if the latter happens, in preventing adhesion of the epoxy to the Pb surface, make it imperative to remove all traces before the application of the next layers of construction and the use of epoxy. Upon delamination testing of Module 1, it separated at the very first Pb sheet and examination of the surfaces indicated poor surface preparation and weak spots. Further testing of identical construction of Pb/SciF/Epoxy mixtures using special fixtures to measure tensile strength of the bond assure that the epoxy bond is much stronger than the weight of the module. These tests prove that the epoxy is strong enough to sustain the module weight, however, surface preparation before application of the epoxy and the complete removal of all traces of petroleum jelly is an operation of particular significance.

Alternative methods of protecting the Pb surface from epoxy migration and/or preventing delamination will be tested. For the former, a thin teflon film may be used to cover the top surface of the last layer of Pb before pressing and curing. The film must cover, however, all the grooves under pressure so that even if epoxy migration takes place through capillary action, it will be prevented from sticking to the Pb surface. Delamination, over time, may be prevented by the use of thin Al tape wrapping the modules at three locations, a technique used by KLOE. Delamination is only a serious concern if it happens during handling, transportation and mounting of the modules because once the BCAL is mounted on its space-frame and inserted into the solenoid, it becomes a self supporting structure.

To establish the centerline for construction, a 0.5mm deep trench is grooved along the major axis of the Aluminum base plate. Optical epoxy was used to glue a single fiber in the groove. After it dries, an industrial two compound, opaque epoxy was used to glue the first lead sheet to the Al plate, carefully aligning it with the guide fiber.

B.2.2 Dimensional uniformity of the matrix

Although the step-pyramid design saves a significant amount of green scintillating fibers (~ 500 km) and Pb, it requires more care in the building up phase of the matrix. Module 1 with its rectangular construction needed only few alignment jigs to keep it perpendicular to the base plate. Furthermore, even minor deviations in a few layers were no problem because the final machining to the $3.75°$ taper angle corrects any such misalignments among layers. However, Module 2 required careful alignment of each step layer of 1.25 cm thickness to be placed 1.00 cm from the edge of the layer below it. The design is not forgiving because any misalignment will create gaps when the module is machined. This is what happened, in fact, with Module 2 and in order to preserve the correct angles and uniformity, Module 2 was machined narrower than originally planned for.

The solution is more care during construction, not always an easy task over years of construction and with many different student labor crews. Teflon alignment jigs bolted along the length of the space frame, and incorporating the *negative* of the step-pyramid dimensions, will be incorporated to assure all layers have their edges parallel to the layer below and are at the correct distance from the edge. Finally, the layers will be made a little wider than the layers in Module 2 to allow for correct final dimensions after machining, even if minor imperfections occur during module construction.

B.3 Construction timelines issues

1. It is important for the epoxy used for the first few layers of the matrix built - at the beginning of each construction period - to be fluid enough to flow under the pressure applied by the pistons during the curing phase. The excess epoxy then flows toward the ends of the module following the tracks, defined by space between the fibers and the grooves on the Pb sheets, resulting in uniform distribution of epoxy and allowing the lead grooves and the fibers to settle uniformly under piston pressure resulting in negligible variations in matrix thickness across the module. Experience has shown that an experienced crew of four can lay down approximately eight layers of Pb, SciFi and Epoxy before the operation ceases and the matrix is pressed and left to cure. On average, this corresponds to 1.0 cm of matrix built-up.

2. The Pb comes either in rolls of approximately $1,200$ kg or sheets of specified length. Width is defined by industry standards and the one selected is based on minimization of wastage since the width of each sheet of Pb to be cut for the module construction is fixed. The Pb sheets, then have to be mounted on a custom-designed and built table and cut to strips of specific width and length for the matrix construction. These strips are then cleaned with ethyl alcohol and fed into the swaging machine to be grooved. They are inspected for straightness and minor curvatures corrected, marked for orientation and side to avoid stacked tolerances during matrix building and rolled around PVC pipe cores for storage and transportation.

3. The fibers need to be inspected for visual defects and minimum length. Then the exact number required to fit the number of grooves on the Pb strip for that particular layer of the matrix is separated, bundled and labeled. This operation, when it takes place before actual construction, saves valuable time during the construction due to the limited time (less than two hours) the epoxy is fluid enough to work with. The fiber sorting operation is best done on a custom-designed table with conductive surface (copper sheet or foil) grounded to remove any dust collecting static electricity built up during handling, even with anti-static gloves.

4. At normal room temperature and humidity levels, an eight-hour time period must pass before the epoxy is hard enough to remove the Al pressure plate and prepare the top surface of the last sheet of

grooved Pb for application of epoxy and SciFi to start the building of the matrix again. During these eight hours, the matrix is under the pressure applied by the 20 pistons.

Taking all the operations into account and the time it takes for each, with the use of two parallel press-frames and a crew of five or six persons, a sustained rate of production of two modules per month is possible. All timelines for the BCAL part of the project are based on this time budget.

C BCAL Simulation Tools

C.1 Overview

- *GEANT:* The GBCAL program is based on GEANT and is flexible in the sense that it can be used to simulate the behavior of a a single BCAL module or any number of modules up to the full 48 in the production phase, and with differing readout segmentation. GBCAL incorporates a detailed description of the Pb/SciFi Matrix, as a result of microscope-based measurements of the matrix of the first full-scale prototype module (Module 1). With about 15,000 fiber volumes in the GEANT geometry description of a single module, plus the layers of lead, optical epoxy rings and boxes, the simulation is very intensive in CPU consumption. However, simulating the exact geometry confers the benefit of determining intrinsic properties of the matrix, such as the sampling fraction, and either entering these results as constants or in parametrized form into the full Hall D GEANT (HDGEANT) simulation and tracking Monte Carlo, where CPU economy is required. For a schematic and details of the geometry the reader is directed to Figure 2.3.

- *FLUKA:* Recently, we have embarked on a parallel effort using the simulation package FLUKA (v. 2006.3b). The exact geometry has been coded into FLUKA as well, and initial simulations of the longitudinal shower deposition profiles are in agreement with those from GBCAL. The objective is to compare the results from the two codes in terms of accuracy and speed of simulation.

- *GUIDEIT:* The optical ray-tracing package GuideIt was used to simulate optical photons in single- and double-clad fibers of the type used in the construction of our prototype modules.

C.2 Energy deposition in Pb, SciFi and Glue

Photons from the GEANT particle gun and from the reaction $\gamma + p \rightarrow \eta + \pi^0 + p \rightarrow (\gamma + \gamma) + (\gamma + \gamma) + p$, generated via the *genr8* phase space distributed event generator, were used to simulate the deposited energy in the volumes of the Pb/SciFi/Glue matrix [48]. Most protons from this reaction carry a comparatively small amount of the momentum and are produced mainly at large angles with respect to the beam direction giving smaller amounts of energy deposited in the lead and scintillating fibers. On the other hand, the η and π^0 decay photons travel mostly forward and carry the largest part of the energy. Only the photons emitted at larger than $10°$ can enter the BCAL.

E_γ (MeV)	R_{Pb}	R_{SciFi}	R_{Glue}	Total	R'_{Pb}	R'_{SciFi}	R'_{Glue}	Total
	versus photon energy (%)				versus energy deposited (%)			
200	77.4	11.9	3.8	93.1	83.1	12.8	4.1	100
500	77.1	11.8	3.8	92.7	83.2	12.7	4.1	100
1000	76.7	11.7	3.8	92.2	83.2	12.7	4.1	100
Phase Space	81.2	12.1	3.9	97.2	83.5	12.5	4.0	100

Table C.1: Percentage of the energy deposited in the lead, scintillating fibers and glue of the module by the photons of 200, 500 and 1000 MeV energies incident on the center of the module and perpendicular to its face, versus photon energy. The primed quantities are determined versus energy deposited in the module. The last row shows the mean percentage of the energy deposited by the η and π^0 decay photons.

The fraction of energy deposited is shown in the first three rows of Table C.1 for photons with fixed energies incident at the center of the module and perpendicular to the face of the module, versus the photon energy.

(The primed quantities are determined with respect to the energy deposited in the module.) As can be seen from the first three rows of the fifth column, the total ratio is ~93% with the remaining ~7% of the energy exiting from the module. Of that, ~3.5% leaks out the sides (but of course this energy would enter into an adjacent modules and be recovered) and another ~3.5% exits the rear. In reality photons will enter the module at different angles and positions. To that end, phase space distributed events were generated for the above reaction at E_γ=9 GeV and are shown in the last row of the table.

C.3   Energy leakage simulations

Detailed simulations were carried out to study the energy leakage from the four sides of the module [49, 5] used in the Hall-B beam tests. Incident photon energies were simulated in the beam test range of 150-650 MeV and at different angles, with the results shown in Table C.2. 'Front' refers to events that 'splash' off the front face of the module, with only a fraction of their energy deposited in the module and the remainder deposited in a module(s) located diametrically opposite to the initially struck module, in the full 48-module configuration. The fraction of energy lost in this manner increases as the polar angle of the incident particle decreases; this behavior is opposite to those events leaking out the rear for which the fraction lost decreases with decreasing angle, a consequence of a larger radiation length at small angles.

E_γ	θ	E_{leak}/E_γ				
(MeV)	(degrees)	Front	Rear	Top	Bottom	Total
650	90	0.6	3.4	1.4	1.3	6.7
	45	0.8	0.9	1.5	1.5	4.6
	20	3.1	0.5	1.4	1.3	6.4
500	90	0.6	3.1	1.4	1.4	6.4
	45	0.9	0.9	1.5	1.4	4.7
	20	3.5	0.5	1.4	1.4	6.8
200	90	0.7	2.0	1.7	1.7	6.3
	45	1.2	0.9	1.6	1.7	5.4
	20	4.4	0.5	1.5	1.5	8.0

Table C.2: The simulated percentage of energy leaking out the four sides of a single BCAL module for various incident photon energies and angles.

C.4   Sampling fraction

The GBCAL code was used to simulate the BCAL's sampling fraction, based both on the photon energy and, more meaningfully, on the energy deposited in the module [10]: $f_\gamma = E_{SciFi}/E_\gamma$ and $f = E_{SciFi}/E_{module}$ where E_{SciFi} is the energy deposited in the scintillating fibre core, E_γ is the incident photon energy and E_{module} is the energy deposited in the module. The former quantity averages out to 11.8% and the latter to 12.5% in the 150-650 MeV Hall-B beam test photon energy range. The energy-deposited sampling fraction f depends only on the internal geometry of the module, is independent of the amount of energy lost as leakage out the sides of the module and is the number coded as a parameter for the full HDGEANT simulation.

Simulations were also carried out in the 10-50 MeV photon energy range and with the incident photon angle varying from 20-90° (90° is perpendicular to the module). The sampled energy and angular distributions were flat. A circular beam spot size of 5 mm was used so that the simulations would not be sensitive to

fiber placement within the module. This has small effect (a few percent) at the low energies on the sampling fraction that ranged from 11.2-11.7% over the 10-50 MeV energy range. Poisson functions fit the deposited energy sampling fraction very well at the low energies, whereas Gaussians work well above 50 MeV. The sampling fraction (f) varied from 10.5-11.7% between $\theta = 20°$-$90°$ but was independent of the energy slice, for energies less than 50 MeV. Finally, simulations were run with a distribution uniform in photon energy from 10 MeV up to 1 GeV perpendicular to the module. The sampling fraction (f) fluctuations were simulated as a function of energy and were found to follow $\sigma_f/f = 4.6\%/\sqrt{E} \oplus 3.2\%$.

C.5   Fractional energy deposition

An important study towards the Monte Carlo validation to data is the examination of the fractional energy deposition in the six layers and three sectors from the Hall-B beam tests. Each end of the module had 18 readout segments, equal in area and arranged in a matrix of 6×3 (depth $\times$ azimuthal), so that we could study the pattern of energy deposition among the segments along and perpendicular to the beam direction, respectively. An initial comparison of GBCAL to the data reveals that whereas the comparison is favorable at photon energies above ~250 MeV, below that discrepancies exist, possibly related to an incomplete implementation of energy deposition thresholds in the Monte Carlo and of the pedestal treatment. This work is ongoing.

C.6   Charged particle energy deposition

MC studies are underway to investigate the energy deposition in the BCAL readout layers for particle species other than photons or e^+e^-, such as protons, charged pions and neutrons as a function of incident momentum. Among these, 500 MeV/c protons show a strikingly distinct pattern of enery deposition as compared to charged pions, a feature that will further aid the PID separation between pions and protons from the BCAL's TOF. This work is ongoing.

C.7   Pre-radiator for BCAL

We simulated a tungsten pre-radiator in front of the calorimeter to examine its effect on the energy leakage out the rear of the BCAL, on the shower maximum, and on the energy resolution and threshold [50]. Adding a tungsten sheet in front of the BCAl is advantageous mechanically. Simulations have been carried out with incident photons of various energies hitting the module perpendicularly at the mid-point of its length. The effect of the pre-radiator on the longitudinal shower profile was examined for different incident photon energies and various thicknesses (4-10 mm) of the pre-radiator. For 100 MeV initial energy and 4 mm thick pre-radiator the shower maximum occurs inside the module but for a 5 mm thickness it occurs inside the pre-radiator. For 500 MeV photons the shower maximum occurs inside the module for all studied pre-radiator thicknesses. Drawbacks of the studied pre-radiator thicknesses is that they raise the BCAL detection threshold considerably above its current design of 40 MeV whereas they do not significantly reduce the energy leaking from the rear, for perpendicular photons. This work is ongoing with studies at different incident angles and on the energy resolution.

C.8 Optical simulation of double-clad fibers

The optical ray-tracing package GuideIt was used to simulate optical photons in single- and double-clad fibers [51]. The trapping efficiency (capture ratio) of optical photons for the BCAL double-clad fibers was simulated and was found to be on average 9.3%, in between the theoretical limits of 5.6% when considering meridional rays alone (those traveling along an axial plane) and 10.6% for meridional plus skew rays (those spiraling down the fiber) [8]. Finally, other quantities such as timing spread and number of bounces at all optical interfaces were also simulated, with air and optical glue surrounding the fibers, respectively, and with different values of optical roughness and light attenuation, to further our understanding of the physical processes involved.

C.9 Pending Monte Carlo Tasks

1. Monte Carlo Validation using the Hall-B beam test data.

   (a) Energy deposition profiles for photons for various angles and positions along the module's length;
   (b) Energy and timing resolution from MC;
   (c) Threshold energy; and
   (d) Effects due to pre-radiator.

2. FLUKA versus GEANT: lateral and longitudinal profile comparison.

3. Energy deposition profiles and patterns for charged particles (protons, pions) and neutrons.

4. Simulate lead sheets with different thickness (to study varying the sampling fraction).

References

[1] L. Tortora. The KLOE detector and physics program. *Nucl. Phys. Proc. Suppl.*, 78:157–162, 1999.

[2] F. Ceradini. The DAPHNE Phi factory: Programme and status. *Nucl. Instrum. Meth.*, A384:72–78, 1996.

[3] Z. Papandreou. BCAL calorimetry response. Technical report, GlueX Collaboration, 2007. GlueX-doc-840-v2.

[4] Z. Papandreou et al. Request for beam time in Hall B to measure energy and time resolution of the BCAL prototype module. Technical report, GlueX Collaboration, 2006. GlueX-doc-620-v1.

[5] R. Hakobyan, Z. Papandreou, G. Lolos, and B. Leverington. BCAL simulations for the Hall B tests. Technical report, GlueX Collaboration, 2007. GlueX-doc-796-v1.

[6] A. Semenov, Z. Papandreou, and I. Semenova. Analysis of amplitude information from 2006 BCAL cosmics runs. Technical report, GlueX Collaboration, 2007. GlueX-doc-845-v4.

[7] St. Gobain Crystals scintillating optical fibers brochure 605.

[8] Z. Papandreou. Scintillating fiber trapping efficiency. Technical report, GlueX Collaboration, 2007. GlueX-doc-918-v2.

[9] C. Kourkoumelis. Analysis of the cosmic ray runs from the BCAL test at JLab. Technical report, GlueX Collaboration, 2007. GlueX-doc-836-v1.

[10] B. Leverington. Sampling fraction fluctuations. Technical report, GlueX Collaboration, 2007. GlueX-doc-827-v3.

[11] M.J. Berger and S.M. Seltzer. Tables of energy losses and ranges of electrons and positrons. Technical report, NASA, Washington, DC, 1964.

[12] B. Rossi. *High Energy Particles.* Prentice-Hall, Inc., Engelwood Cliffs, NJ, 1952.

[13] B. Leverington. Analysis of the BCAL beam tests. Technical report, GlueX Document, 2007. GlueX-doc-804-v4.

[14] G. Koleva. Beam Tests for the GlueX Barrel Calorimeter Prototype. Technical report, M. Sc. Thesis (U. of Regina), 2006. GlueX-doc-824-v1.

[15] D. I. Sober et al. The bremsstrahlung tagged photon beam in Hall B at JLab. *Nucl. Instrum. Meth.*, A440:263–284, 2000.

[16] A. Dzierba. Calibrating BCAL with cosmic rays. Technical report, GlueX Collaboration, 2007. GlueX-doc-834-v2.

[17] A. Antonelli et al. Measurements of light yield, attenuation length and time response of long samples of 'blue' scintillating fibers. *Nucl. Instrum. Meth.*, A370:367–371, 1996.

[18] N. Kolev et al. Dependence of the spatial and energy resolution of BCAL on segmentation. Technical report, GlueX Document, 2007. GlueX-doc-659-v2.

[19] E. Smith. Magnetic fields at the location of detector PMT's. Technical report, GlueX Collaboration, 2007. GlueX-doc-912-v3.

[20] P. Ioannou, C. Kourkoumeli, G. Lolos, and G. Voulgaris. BCAL readout utilizing field-resistant PMT's. Technical report, GlueX Collaboration, 2006. GlueX-doc-712-v2.

[21] E. Smith. Readout of the barrel calorimeter based on conventional photomultiplier tubes. Technical report, GlueX Collaboration, 2007. GlueX-doc-832-v3.

[22] E. Smith. Light guide collection for BCAL outer layers. Technical report, GlueX Collaboration, 2008. GlueX-doc-959-v3.

[23] Z. Papandreou. SiPM Primer. Technical report, GlueX Collaboration, 2007. GlueX-doc-741-v2.

[24] G. Lolos. A critical review of BCAL readout options. Technical report, GlueX Collaboration, 2007. GlueX-doc-799-v1.

[25] G. Lolos. Brief review of BCAL and SiPM systems. Technical report, GlueX Collaboration, 2007. GlueX-doc-807-v1.

[26] G. Lolos. BCAL readout review 2007. Technical report, GlueX Collaboration, 2007. GlueX-doc-808-v3.

[27] G. Lolos. Brief report on SiPM array developments. Technical report, GlueX Collaboration, 2007. GlueX-doc-848-v2.

[28] C. Zorn. Notes on the latest SiPM developments. Technical report, GlueX Collaboration, 2007. GlueX-doc-899-v1.

[29] C. Zorn. SiPM Presentation at the 2007 IEEE NSS/MIC Conference. Technical report, GlueX Collaboration, 2007. GlueX-doc-913-v1.

[30] G. Lolos. Testing report of SiPM arrays under Phase I. Technical report, GlueX Collaboration, 2007. GlueX-doc-926-v4.

[31] C. Zorn. Some results with the new trenched A20H SiPM sample. Technical report, GlueX Collaboration, 2008. GlueX-doc-932-v1.

[32] C. Zorn. Tests of SensL silicon photomultiplier prototypes at Jefferson Lab. Technical report, GlueX Collaboration, 2008. GlueX-doc-961-v1.

[33] A. Dzierba, G. Lolos, and Z. Papandreou. BCAL scintillating fiber emission spectra analysis. Technical report, GlueX Collaboration, 2007. GlueX-doc-924-v1.

[34] E. Smith. Specification and evaluation of BCAL readout options. Technical report, GlueX Collaboration, 2007. GlueX-doc-795-v16.

[35] M. Adinolfi et al. Calibration and reconstruction performances of the KLOE electromagnetic calorimeter. *Nucl. Instrum. Meth.*, A461:344–347, 2001.

[36] M. Adinolfi et al. The KLOE electromagnetic calorimeter. *Nucl. Instrum. Meth.*, A494:326–331, 2002.

[37] M. Adinolfi et al. The KLOE electromagnetic calorimeter. *Nucl. Instrum. Meth.*, A482:364–386, 2002.

[38] M. Adinolfi et al. The trigger system of the KLOE experiment. *Nucl. Instrum. Meth.*, A492:134–146, 2002.

[39] F. Ambrosino et al. Data handling, reconstruction, and simulation for the KLOE experiment. *Nucl. Instrum. Meth.*, A534:403–433, 2004.

[40] A. De Santis. Misura della sezione d'urto del processo $e^+e^- \rightarrow \omega\pi^0 \rightarrow \pi^0\pi^+\pi^-\pi^0$ con il rivelatore KLOE a DAFNE e sua influenza per gli studi interferometria quantistica con i mesoni K neutri. Doctoral Thesis - University of Rome, 2004.

[41] A. AloIsio et al. Study of the decay $\phi \rightarrow \pi^0\pi^0\gamma$ with the KLOE detector. *Phys. Lett.*, B537:21, 2002.

[42] A. Aloisio et al. Study of the decay $\phi \rightarrow \eta\pi^0\gamma$ with the KLOE detector. *Phys. Lett.*, B536:209, 2002.

[43] B. Klein et al. BCAL progress and construction report. Technical report, GlueX Collaboration, 2004. GlueX-doc-333-v1.

[44] T. Summers. Premature epoxy stiffening tests and solutions. Technical report, GlueX Collaboration, 2004. GlueX-doc-266-v1.

[45] G. Koleva. Surface scan of the 2-m BCAL module. Technical report, GlueX Collaboration, 2004. GlueX-doc-271-v1.

[46] R. Filby and B. Jasper. UV exposure of fibers and construction of BCAL module 1. Technical report, GlueX Collaboration, 2004. GlueX-doc-331-v1.

[47] Z. Papandreou. Electro-pneumatic press for BCAL - a video in .avi format. Technical report, GlueX Collaboration, 2004. GlueX-doc-182-v1.

[48] R. Hakobyan, Z. Papandreou, G. Lolos, and B. Leverington. Simulation of the GlueX BCAL Calorimeter. Technical report, GlueX Collaboration, 2005. GlueX-doc-529-v5.

[49] R. Hakobyan and Z. Papandreou. BCAL energy deposition and leakage. Technical report, GlueX Collaboration, 2007. GlueX-doc-829-v1.

[50] S. Katsaganis. BCAL and Tungsten. Technical report, GlueX Collaboration, 2005. GlueX-doc-841-v1.

[51] I. Chatziantonaki. Simulation of double-clad fibers using the GuideIt ray-tracing package. Technical report, GlueX Collaboration, 2007. GlueX-doc-766-v1.